View metadata, citation and similar papers at core.ac.uk

brought to you by CORE

provided by NASA Technical Reports Server

Seasonal and interannual variabilities in tropical tropospheric ozone

J. R. Ziemke[1]
Software Corporation of America, Lanham, Maryland

S. Chandra
NASA Goddard Space Flight Center, Greenbelt, Maryland

Received November 7, 1997; revised May 4, 1998; accepted May 7 1998.

Submitted to *Journal of Geophysical Research*, 1998.

Short title: TOMS CCD 1979-1998 TROPICAL TROPOSPHERIC OZONE

[1]Also at NASA Goddard Space Flight Center, Greenbelt, Maryland.

Abstract.

This paper presents a detailed characterization of seasonal and interannual variability in tropical tropospheric column ozone (TCO). TCO time series are derived from 20 years (1979-1998) of total ozone mapping spectrometer (TOMS) data using the convective cloud differential (CCD) method. Our study identifies three regions in the tropics with distinctly different zonal characteristics related to seasonal and interannual variability. These three regions are the eastern Pacific, Atlantic, and western Pacific. Results show that in both the eastern and western Pacific seasonal-cycle variability of northern hemisphere (NH) TCO exhibits maximum amount during NH spring whereas largest amount in southern hemisphere (SH) TCO occurs during SH spring. In the Atlantic, maximum TCO in both hemispheres occurs in SH spring. These seasonal cycles are shown to be comparable to seasonal cycles present in ground-based ozonesonde measurements. Interannual variability in the Atlantic region indicates a quasi-biennial oscillation (QBO) signal that is out of phase with the QBO present in stratospheric column ozone (SCO). This is consistent with high pollution and high concentrations of mid-to-upper tropospheric O_3-producing precursors in this region. The out of phase relation suggests a UV modulation of tropospheric photochemistry caused by the QBO in stratospheric O_3. During El Niño events there is anomalously low TCO in the eastern Pacific and high values in the western Pacific, indicating the effects of convectively-driven transport of low-value boundary layer O_3 (reducing TCO) and O_3 precursors including H_2O and OH. A simplified technique is proposed to derive high-resolution maps of TCO in the tropics even in the absence of tropopause-level clouds. This promising approach requires only total ozone gridded measurements and utilizes the small variability observed in TCO near the dateline. This technique has an advantage compared to the CCD method because the latter requires high-resolution footprint measurements of both reflectivity and total ozone in the presence of tropopause-level cloud tops.

1. Introduction

It is generally recognized that the seasonal maximum in tropospheric column ozone (TCO) in the tropical south Atlantic region is related to intense biomass burning in Africa and Brazil during southern spring [*Crutzen and Andreae*, 1990; *Fishman et al.* 1990, 1991, 1992; *Watson et al.* 1990]. A number of papers published in the special issue of the Journal of Geophysical Research [e.g., *Fishman et al.*, 1996; *Thompson et al.*, 1996; *Krishnamurti et al.*, 1996; *Jacob et al.*, 1996], as a part of the Transport and Atmospheric Chemistry near the Equator-Atlantic (TRACE-A) campaign, have provided a broader understanding of the relationship between biomass burning and tropospheric ozone in the tropics. These studies suggested that the presence of biomass burning in South America and southern Africa is a primary source of ozone precursors (e.g., CO, NO_x and hydrocarbons) which can lead to a 10-15 DU increase in tropospheric column ozone in this region. Similar conclusions have also been arrived at by *Wang et al.*, [1998a] and *Brasseur et al.* [1998] using three-dimensional transport models.

The interpretation of the south Atlantic tropical ozone anomaly in terms of biomass burning is complicated by the fact that a number of meteorological parameters also show a predominant zonal wave 1 structure similar to TCO, thus raising the possibility that the anomaly may be of meteorological origin [e.g., *Krishnamurti et al.*, 1993; *Ziemke and Chandra*, 1998]. For example, the transport model used by *Krishnamurti et al.* [1993] for October months showed that tropospheric subsidence and horizontal transport of air (caused by persistent planetary scale circulation) in the south Atlantic region can produce an ozone peak in this region even in the absence of biomass burning. The anomalous increase of 10-20 DU in TCO in the Indonesian region during 1997-1998 El Niño [*Chandra et al.*, 1998] clearly highlights the difficulty of delineating the relative importance of dynamical and biogenic processes. During this period, there were large-scale fires in the tropical rainforests of Indonesia. There was also a major

shift in the atmospheric convection pattern from the western to the eastern Pacific causing O_3 to vary inversely as water vapor. As suggested by *Chandra et al.* [1998], the increase in TCO and the decrease in tropospheric water vapor in the Indonesian region during the 1997-98 El Niño may have been caused by a combination of large -scale circulation processes associated with the shift in the tropical convection pattern and the surface/boundary layer processes associated with the fires in this region.

It is apparent that to gain further insight into the relative role of photochemical and transport processes in the tropical troposphere one needs to better characterize ozone variability over a longer period in terms of perturbations associated with biomass burning, convective activity in the tropical Pacific region, and changes in column ozone above the tropopause. The latter affects solar UV radiation entering the troposphere and alters the photochemical and radiative properties of the troposphere [e.g, *Haigh*, 1996; *Hansen et al.*, 1997]. *Chandra et al.* [1999] have shown that the solar-cycle signal in TCO in the marine tropical troposphere is out of phase with stratospheric column O_3. Since the stratosphere is strongly influenced by the quasi-biennial oscillation (QBO), it may also produce interannual variability in the troposphere on a QBO time scale through modulation of UV flux entering the troposphere.

The purpose of this paper is to present the results of such a study based on TCO time series derived from 20 years (1979-1998) of total ozone mapping spectrometer (TOMS) data using the convective cloud differential (CCD) method [*Ziemke et al.*, 1998]. These time series represent monthly values binned to a 5°×5°grid. Tropical convective activity is inferred from the Southern Oscillation index (SOI) and National Oceanic and Atmospheric Administration (NOAA) outgoing longwave radiation (OLR) data [*Liebmann and Smith*, 1996]. Biomass burning events are identified using TOMS aerosol-smoke index (ASI) measurements [*Hsu et al.*, 1996; *Herman et al.*, 1997]. Both OLR and ASI data were also binned to a monthly 5°×5°grid for studying the relative variability of TCO with respect to these parameters.

Our study begins with a description of data and analysis (section 2) followed by a general overview of tropospheric O_3 (section 3), and then annual cycles (section 4), interannual variability (section 5), the recent 1997-1998 El Niño event (section 6), an alternative method of deriving TCO (section 7), and finally a summary (section 8).

2. Data and Analysis Methods

This study uses column O_3 data derived from Nimbus 7 (January 1979 through April 1993) and Earth Probe (July 1996 through August 1998) total ozone mapping spectrometer (TOMS) backscattered ultraviolet measurements. TCO and stratospheric column ozone (SCO) in the tropics were obtained from TOMS data using the convective-cloud differential (CCD) method [*Ziemke et al.*, 1998]. In the CCD method total (i.e., stratospheric plus tropospheric) column O_3 is derived from low reflectivity ($R < 0.2$) measurements and stratospheric column O_3 follows from nearby column O_3 measurements taken above the tops of very high tropopause-level clouds with high reflectivity ($R > 0.9$).

In practice SCO is calculated in the Pacific region where tropopause-level clouds are always present. SCO is derived for every 5° latitude band and averaged over longitudes from 120°E eastward to 120°W. These values are then assumed to be independent of longitude in a given latitude band. This assumption is based on the zonal characteristics of tropical SCO as inferred from Upper Atmosphere Research Satellite (UARS) microwave limb sounder (MLS) and halogen occultation experiment (HALOE) assimilated data [*Ziemke et al.*, 1998]. Measurement uncertainties in TCO from the CCD method are discussed in detail by *Ziemke et al.* [1998]. Largest uncertainties are anticipated to lie in the Atlantic region where the assumption of a zonally invariant stratospheric O_3 column could produce additional errors of several DU in TCO. For all TCO time series shown in this study, 2σ measurement uncertainty errors are estimated to vary approximately uniformly from about 3 DU in the Pacific region up to ~5 DU in

the remote Atlantic.

Examples showing the property of zonal homogeneity of tropical SCO are given in Figure 1 which plots zonal distributions of daily 0-100 hPa SCO derived from HALOE (solid) and co-located EP TOMS total ozone (dashed) for four selected days during and after the recent 1997-1998 El Niño event. Even in daily measurements the approximation of zonal invariance of SCO appears to be qualitatively valid despite robust changes occurring in tropical convection in the Pacific between El Niño year (top two frames) and non-El Niño year (bottom two frames). As shown by *Ziemke et al.* [1998], TCO derived from the CCD method agrees well with available ground-based measurements in the tropics. For example, Figure 2 [not included in *Ziemke et al.*, 1998] shows good qualitative agreement between CCD and ozonesonde TCO time series at both Pacific Samoa (14°S, 170°W) and Nairobi (-1°S, 37°E) in east Africa.

A potential source of error in assuming zonal symmetry of tropical SCO is the temporal and spatial changes in tropopause height. As shown by *Logan* [1998] and also from our own analyses of tropical sonde data, zonal variability of the tropical tropopause is generally only a few hundred meters, equivalent to (at most) ~5-10 hPa change in tropopause pressure. According to *Gage and Reid* [1987], seasonal variability of the tropopause in the tropical Pacific (the region where CCD SCO data are derived) is generally around 1 km (~10 hPa tropopause change) with interannual variability smaller at around a few hundred meters. Table 1 shows seasonally-averaged tropopause pressures, tropopause heights, TCO, and total number of profiles from tropical stations Ascension Island, Natal, Brazzaville, and Samoa. For clarity, mean standard deviations are not included in Table 1. (Standard deviations can be shown to vary for all these tropical stations by ~4-8 hPa for seasonal tropopause pressures, a few hundred meters for tropopause heights, and ~2-4 DU for TCO). Ozonesonde profiles at Ascension Island and Brazzaville are from 1990-1992, while data from Samoa encompass 1984-1989 and 1995-1996 time periods. The longest and most continuous sonde record is at Natal and

spans 1979-1992. Results from Table 1 indicate nearly uniform tropopause pressures (~100 hPa) and tropopause heights (~17 km) year round in the tropics. As shown by *Ziemke and Chandra* [1998] and as inferred from Table 1, fluctuations (up to 10 hPa, or 1 km) of the tropopause in the Pacific at Samoa produce at most around 2 DU change in TCO. We also note that TCO amounts given in Table 1 corroborate the existence of the persistent tropical zonal wave 1 distribution [e.g., *Fishman and Larsen*, 1987; *Ziemke et al.*, 1996; Hudson and Thompson, 1998] with high values in the Atlantic and low values in the Pacific.

3. Three Tropical Regions with Distinctly Different Characteristics

The variability of TCO in the tropics can be generalized by simply examining TCO time series from three different regions that exhibit distinctly different behavior. Figure 3 shows TCO monthly-mean time series (dark curves) evaluated along the Equator in the eastern Pacific (left), Atlantic (middle), and western Pacific (right) for January 1979-December 1992. Also shown are regression model fits (light curves, discussed below) incorporated to help quantify the different mechanisms likely responsible for monthly to decadal variations. For plotting, all time series in Figure 3 were smoothed with a 3-month running average. The time series in this analysis included only data from Nimbus 7 TOMS. Data from EP TOMS, which became available in late July 1996, show about +5 DU offset with respect to Nimbus 7 in derived TCO. The cause of this difference is currently not fully understood but is being investigated. Because of this bias, data from EP TOMS cannot be easily combined with data from Nimbus 7 TOMS in regression analyses.

The linear regression model used in this study, similar to those described by *Randel and Cobb* [1994] and *Ziemke et al.* [1997], is as follows:

$$\Omega(t) = \alpha(t) + \beta(t)\ t + \gamma(t)\ \mathrm{QBO}(t) + \delta(t)\ \mathrm{solar}(t)$$
$$+\epsilon(t)\ \mathrm{ENSO}(t) + \mathrm{R}(t). \qquad (1)$$

In (1), Ω is column ozone, t represents the month index (t=1,2,...,168, corresponding to January 1979 through December 1992), and $\alpha, \beta, \gamma, \delta$, and ϵ are time-dependent regression coefficients given (at most) by a constant plus 12-month, 6-month, and 4-month cosine and sine harmonic series as used by *Randel and Cobb* [1994] and *Ziemke et al.* [1997]. The seasonal-cycle coefficient α was modeled by the 7-term harmonic expansion $c_0 + \sum_{j=1}^{3}[c_j \cos(2\pi jt/12) + s_j \sin(2\pi jt/12)]$, where c_j and s_j are constants. Each of the other coefficients in (1) were all modeled using a amaller 5-term harmonic expansion given by $c_0 + \sum_{j=1}^{2}[c_j \cos(2\pi jt/12) + s_j \sin(2\pi jt/12)]$. The error in (1) is the residual series R(t) and the decadal linear trend is given by the coefficient β. Solar(t) in (1) represents the solar proxy (10.7-cm solar flux series), and ENSO(t) is given by the Tahiti minus Darwin sea level pressure time series. QBO(t) in (1) represents the quasi-biennial oscillation (QBO) proxy derived from Singapore (1°N, 140°E) zonal winds using the empirical orthogonal function (EOF) approach of *Randel et al.* [1995] [described in an earlier study by *Wallace et al.*, 1993]. For TCO a 3-month lag was applied to QBO(t); this time lag was found to provide maximum anticorrelation between TCO and SCO in the tropics, a scenario indicating a possible UV modulation of tropospheric O_3 photochemistry by QBO-induced changes in SCO. This 3-month lag is comparable to e-folding decay time scales for O_3 in the upper troposphere [e.g., *Jacob et al.*, 1996]. Error analysis for the regression coefficients involved a multivariate method with an additional modulation of coefficient errors using the seasonal cycles present in residual time series. This multivariate approach showed nearly identical monthly coefficient critical values and critical regions when tested against the more extensive

Monte Carlo results of *Ziemke et al.* [1997] that included additional errors (~2-5%) for all proxy terms in (1).

Because the focus of our study is the characterization of seasonal and interannual changes in tropical TCO, we do not discuss in detail the solar cycle and linear trend terms in (1). We instead refer the reader to the previous study by *Chandra et al.* [1999] regarding decadal variabilities in tropical TCO which indicated a statistically significant solar cycle (anticorrelated with F10.7) and essentially zero trends. That study indicated that the solar signal in TCO (~2-3 DU peak-to-peak) could not be explained from photochemistry alone, and is possibly caused instead by subtle changes in transport over a solar cycle.

Figure 3 indicates consistently high values in the Atlantic compared to the Pacific, where even minimum values of TCO in the Atlantic region are generally greater than largest values in the Pacific. This identifies what several previous studies have referred to as a primarily zonal wavenumber 1 pattern in tropical tropospheric O_3 first identified by *Fishman and Larsen* [1987].

Table 2 shows the variances explained by each of the regression terms in (1) for the three time series plotted in Figure 3. These results indicate that the dominant variability (~40-50%) in the Pacific is interannual and appears to be related to El Niño and La Niña events whereas in the Atlantic the leading source is the annual cycle that explains ~50% of total variance. In the Atlantic there is also evidence of an interannual variability (~9%) associated with the QBO. In the following sections we will attempt to quantify these detected variabilities in TCO beginning with the annual cycle.

4. Annual cycles

Figure 4 shows 1979-1992 mean annual-cycles ($\alpha(t)$ in (1)) for six northern hemisphere (NH) and southern hemisphere (SH) gridpoints coinciding with the same three longitudes in Figure 3. As *Ziemke et al.* [1998] showed, and as also seen in Figure

4, TCO in the SH is largest around SH springtime. Seasonal variability and TCO amount are both smallest in the SH western Pacific. Figure 4 indicates that NH TCO maximizes around NH springtime in both the eastern and western Pacific and in autumn in the central Atlantic. A remarkable result from Figure 4 is a large difference between hemispheres in the seasonal variability of SCO. SCO in the NH shows a large annual cycle change (~30 DU peak-to-peak), implying that seasonal variability in total column ozone in the NH tropics is driven mostly by changes in stratospheric O_3. In comparison, seasonal variability in SH total column O_3 appears largely driven by tropospheric O_3.

Ziemke et al. [1998] previously compared CCD and ozonesonde TCO measurements at Samoa, Natal, Brazzaville, and Ascension Island in the SH tropics. Unfortunately extensive comparisons are not possible in the NH tropics because of lack of sufficient ozonesonde data. Although located at a more northerly latitude, Hilo (20°N, 155°W) is one station that has enough sonde data to derive a seasonal climatology for TCO. In addition, despite a reduced number of high-reflectivity cloud scenes at 20°N compared to the lower latitudes, the CCD method still yields enough data to also provide a seasonal climatology of TCO for comparison. These two climatologies are plotted together in Figure 5. Both indicate a similar seasonal cycle with peak values occurring in the spring season. We note that some of the features in the seasonal cycles in Figures 4 and 5 are well simulated in the 3-D photochemical transport model results of *Wang et al.* [1998b].

Figure 6 shows horizontal cross sections of annual means and annual amplitudes in TCO derived from $\alpha(t)$ in (1). In Figure 6 (top), largest TCO values greater than 36 DU occur in the south Atlantic, with smallest values (less than 22 DU) in the Pacific near the dateline. Annual-mean amplitudes (Figure 6, bottom) indicate values up to 7 DU over eastern Brazil and 5-6 DU over southern Africa. The 5-7 DU annual amplitudes (i.e., 10-15 DU peak-to-peak seasonal changes) in Figure 6 (bottom) over these regions provide a mean upperbound to seasonal variability in TCO.

Because of the persistence of the O_3 maximum in the south Atlantic and the

ubiquitous nature of seasonal changes in CCD TCO present in Figure 6 (bottom), it is difficult to justify biomass burning as the fundamental contributing factor. Seasonal changes in dynamical transport affect tropospheric O_3 photochemistry by altering concentrations of O_3 producing and destroying precursors. We also note that the model by *Wang et al.* [1998a] included sources other than biomass burning such as the burning of fossil fuels, lightning and soil emissions. In the next section we examine interannual variabilities of TCO in the tropical Atlantic and Pacific regions and establish plausible explanations for those changes.

5. Interannual Variability

A new and important result from this study is the characterization of interannual variabilities in tropical TCO. The comparison of interannual variabilities present in TCO and other geophysical parameters offers insight that cannot be gained by examining only seasonal cycles.

Interannual variabilities in TCO associated with both QBO and ENSO are shown in Figure 7. Given are annual averages of γ and ϵ from (1) with shading indicating regions where these coefficients are not different from zero at the 2σ level. Figure 7 (top) plots the QBO coefficients which appear statistically significant in the Atlantic region. The signature for ENSO (Figure 7, bottom) shows a dipole pattern centered just west of the dateline. We note that this Pacific dipole pattern and inflection region for ENSO near 165°-170°E is also present in similar 1979-1992 regression analyses of both NOAA OLR and Goddard GEOS-1 surface temperature data (figures not shown).

Physical amplitudes (in DU) in TCO attributed to QBO and ENSO can be estimated by simply multiplying the mean coefficient values in Figure 7 with QBO(t) and ENSO(t) used in (1). Given ± 35 ms^{-1} extremes present in the EOF QBO wind time series QBO(t), coefficient values of -0.3 to -0.4 seen in Figure 7 (top) in the Atlantic region translate to $\sim$2-3 DU peak-to-peak changes in TCO. For ENSO, TCO changes

during an El Niño or La Niña event are comparable, but slightly larger in amount than QBO. Given 2 hPa extremes present in time series ENSO(t) during either an El Niño or La Niña event, coefficient amplitudes of around 1.5 to 2.0 seen in Figure 7 (bottom) in the western and eastern Pacific region translate to ~3-4 DU anomalies in TCO.

Figure 7 indicates that while interannual variability in the Pacific is dominated by ENSO, variability in the Atlantic region appears to be associated instead with the QBO. The negative sign of $\gamma(t)$ suggests that the QBO in TCO is out of phase with the QBO in SCO with a 3-month phase lag. This is readily seen in Figure 8 which compares the interannual temporal changes in SCO and TCO along the equator at 0°longitude. The time series shown were deseasonalized and extend through August 1998 to include the more recent EP TOMS time period. TCO data for EP TOMS were subtracted by 5 DU to account for the apparent bias with respect to Nimbus 7 (discussed in section 3). In addition, the TCO time series in Figure 8 was lagged by 3 months for maximum anticorrelation with SCO (also discussed in section 3).

Figure 8 suggests an out of phase relationship between SCO and TCO on a QBO time scale over most of 1979-1998 except for a short duration from 1989 to 1991. The out of phase relation suggests that interannual changes in tropospheric O_3 in the tropical Atlantic region is controlled by photochemical processes which are influenced by the UV flux entering the troposphere. The latter is inversely proportional to stratospheric O_3 which is modulated by the QBO. A 3-month phase shift is characteristic of a photochemical time constant for O_3 in the upper troposphere. UV modulation of upper tropospheric photochemistry in the Atlantic may be the result of a more polluted environment compared to the Pacific region.

Both convection and biomass burning seem to have little effect on the interannual variability of TCO in the Atlantic region. This is illustrated in Figure 9 which compares TCO time series with OLR (upper panel) and ASI (lower panel). The conclusion from Figures 8 and 9 is that interannual variability in TCO in the Atlantic region appears

as a manifestation of the QBO in stratospheric O_3, with little influence from either convective activity or biomass burning.

In comparison, both the eastern and western Pacific regions are strongly influenced by tropical convection as seen in Figure 7 (upper panel) and as further illustrated in Figure 10. Figure 10 shows deseasonalized time series of TCO along the equator in the western Pacific (top) and eastern Pacific (bottom). TCO derived from EP TOMS measurements again includes a subtraction of 5 DU with respect to Nimbus 7. There is evidence of an interannual signal in the eastern and western Pacific associated with the 1982-1983, 1987, 1991-1992, and 1997-1998 El Niño events. Recovery of the 1997-1998 El Niño in TCQ and OLR is seen near the end of the record shown, around the months of May and June 1998. Months following June 1998 indicate a shift toward a La Niña condition with larger than average amount of convection in the western Pacific region.

The observed positive anomalies in TCO in the western Pacific during El Niño in Figure 10 are consistent with suppressed convection and less reduction of TCO from vertically transported low boundary-layer O_3 and O_3-destroying agents, while negative anomalies in the eastern Pacific are consistent with enhanced convection and opposite effects as discussed by *Chandra et al.* [1998].

6. The Recent 1997-1998 El Niño event in the Pacific

The recent 1997-1998 El Niño was similar in strength to the 1982-1983 El Nlño but in comparison had greater incidences of uncontrolled wildfires over Indonesia. As a result there were large increases in TCO during the 1997-1998 El Niño caused by the combination of a change in dynamical transport and O_3 generated from the intense biomass burning.

The study by *Chandra et al.* [1998] previously analyzed the impact of the 1997-1998 El Niño on TCO and upper tropospheric H_2O, showing that the signatures in these constituents were consistent with the shift (west to east across the dateline) in convection

and associated surface boundary layer processes. Figure 11 compares tropical maps of TCO between October 1996 (top) and October 1997 (bottom). The October 1996 plot indicates a normal non-El Niño condition with largest TCO in the Atlantic and lowest TCO in the western Pacific. In October 1997 this pattern changed dramatically during El Niño with small TCO in the eastern Pacific and large TCO in the western Pacific over Indonesia. The sizeable ~40-45 DU values of TCO observed over Indonesia in September-November 1997 were similar to typical amounts present in the tropical Atlantic, which is an oceanic region with suppressed convection (including considerable subsidence of air mass) year round.

Relative to the non-El Niño year of 1996, TCO in late 1997 was found by *Chandra et al.* [1998] (and as also inferred from Figure 11) to decrease by 4-8 DU in the eastern Pacific and increase by 10-20 DU in the western Pacific. It was apparent from observed TCO, UARS MLS 215 hPa H_2O, and NOAA OLR that suppressed convection over Indonesia during El Niño resulted in less upward transport of O_3-destroying precursors including H_2O. But suppressed convection and dry conditions also lead to uncontrolled wildfires over Indonesia extending from Sumatera to New Guinea, generating O_3-producing constituents such as CO and NO_x. It was indicated by *Chandra et al.* [1998] that most increase in TCO in the western Pacific was likely caused by suppressed convection and a change in O_3 photochemistry, but we note that a significant portion of the increase may have been caused by O_3 generated by the large-scale uncontrolled burning.

One can estimate TCO amounts generated by the Indonesian wildfires in late 1997 under the premise that O_3 precursors generated from the burning were limited mostly to the lower-most troposphere because of the suppressed convection present over this broad region. We note in comparison that suppressed convection during the biomass burning season at Cuiaba (15.6°S, -56.1°W) in Brazil indicates that O_3 generated from the burning is limited mostly to the boundary layer [*Sahai et al.*, manuscript in

preparation, 1999]. Column O_3 amount ($\Delta\Omega$) between two pressure surfaces P_{low} and P_{high} ($P_{low} < P_{high}$) can be calculated by integrating O_3 volume mixing ratio (X) over pressure from P_{low} to P_{high}: $\Delta\Omega = A \cdot \int_{P_{low}}^{P_{high}} X \, dP$, where A is a constant ensuring units DU in the integration. (A=0.788 DU hPa^{-1} ppmv^{-1} provided that the units for X and P are ppmv and hPa, respectively.) Intense biomass burning over Indonesia during 1993-1994 was studied previously by *Komala et al.* [1996]. In that study O_3 in the troposphere indicated ~20-25 ppbv increase (relative to non-burning months) in lower tropospheric O_3 between ~750 hPa (~2.5 km altitude) and ~1000 hPa (surface). For the extensive 1997 Indonesian fires, if we assume a larger (double) biomass-burning increase in lower tropospheric X between 750 hPa and 1000 hPa of ~25-50 ppbv, the anomaly in TCO associated with the burning would then be 5-10 DU. This amounts to one fourth to one half the ~20 DU increase indicated by *Chandra et al.* [1998].

We now focus our investigation of the duration and recovery of the 1997-1998 El Niño in the tropical western Pacific region where large amounts of TCO occurred during September-November 1997. One can attempt a comparison of the relative impact of convection effects versus biomass burning in the Pacific for this El Niño event by examining coincident measurements of both NOAA OLR and TOMS ASI. In effort to study their possible relationships with tropospheric O_3 it is useful to extend this comparison backward in time to include previous El Niño events such as the similarly intense 1982-1983 episode. Figure 12 compares time series of deseasonalized TCO, OLR, and ASI averaged over the western Pacific from January 1979 through August 1998. Again, 5 DU was subtracted from original TCO data from EP TOMS relative to Nimbus 7.

Although TCO and OLR (Figure 12, top) are coherent over this long time record, so can be said for TCO and ASI (Figure 12, bottom) particularly during the 1982-1983, 1991-1992, and 1997-1998 El Niño events. It is not possible to distinguish from Figure 12 whether dynamical transport and induced changes in O_3 photochemistry dominates

generation of TCO over that of biomass burning during El Niño events because OLR and ASI anomalies are by nature generally positively correlated in this region. During El Niño, OLR in the western Pacific is large because of suppressed convection and the ensuing dryness results in increased amounts of uncontrolled wildfires.

Results in this study indicate that intense biomass burning over the western Pacific during El Niño events generates a considerable amount of tropospheric O_3 but is likely limited to the lower troposphere. Evidence suggests that biomass burning alone does not explain the large increases observed in TCO in the region. Independent of biomass burning, a change in convection in the tropical western Pacific will alter in situ O_3 photochemistry in the troposphere. Conceivably, suppressed convection during El Niño in the western Pacific oceanic region results in an increase in TCO because of reduced transport of both low-value boundary-layer O_3 and O_3-destroying agents including H_2O and OH.

7. A Simplified Method For Deriving Tropical Tropospheric Column Ozone

An important result from this study was identifying the western Pacific near the dateline as a region with small seasonal variability (see Figure 6) and little or no ENSO or QBO interannual signals in TCO (see Figure 7). Because of small variability of TCO in this region, a simplified method is proposed to estimate tropical O_3 distribution from only total ozone gridded measurements. This technique is discussed in detail in the appendix. The direct CCD method in comparison requires high-resolution footprint measurements of both reflectivity and total ozone, and the presence of tropopause-level clouds.

As an example of this extended method, Figure 13 compares 1979-1998 TCO time series between the CCD and simplified method at 10°S in the eastern Pacific,

Atlantic, and western Pacific regions. Also included in these time series are NOAA 11 solar backscatter ultraviolet/2 (SBUV2) total column O_3 measurements for May 1993 through November 1994 to help bridge the gap of missing data between the Nimbus 7 and EP TOMS time periods. Absolute value differences are plotted along the bottom of each frame. Despite simplicity of this technique, Figure 13 shows good agreement between these two methods.

8. Summary

The variability of O_3 in the tropical troposphere can be generalized by simply examining time series from three different regions: the western Pacific, the central Atlantic, and the eastern Pacific. Away from the Atlantic region seasonal variability in NH tropical TCO derived from the CCD method indicates maximum amounts around NH spring months; in contrast, greatest amounts in SH TCO occur around SH spring months. Throughout the central Atlantic there was shown to be a dominant annual cycle with maximum TCO around SH spring. An interesting result was that seasonal variability in NH total column O_3 appears dominated by seasonal changes in stratospheric O_3, in contrast to the SH in which seasonal cycles are driven largely by tropospheric O_3. These regional differences in seasonal-cycles were validated from ozonesonde data in this study and from results of previous investigations.

A new result from this study was a characterization of interannual variabilities in tropical TCO. By comparing interannual variabilities in TCO and other geophysical parameters (e.g., OLR, ASI) we can gain insight not obtainable from examining only seasonal-cycle relationships, which in some cases may seem plausible but may not be true cause and effect. Previous studies have established a seasonal link between biomass burning and tropospheric O_3 in the tropical Atlantic, but our results indicate that these same parameters indicate a very different conclusion for interannual timescales. This study showed that interannual variabilities between biomass burning and tropospheric

O_3 in the Atlantic were incoherent. Instead, interannual variability in TCO indicated a QBO signal that appears out of phase with the QBO present in SCO. This QBO result is consistent with high pollution and high concentrations of O_3-producing precursors in this region in the mid-to-upper troposphere. The out of phase relation suggests a UV modulation of tropospheric photochemistry caused by the QBO in stratospheric O_3.

During El Niño events there exists low values of TCO in the eastern Pacific and high values in the western Pacific. These interannual variabilities in the marine environment appear to be associated with convectively driven upward transport of low-value boundary layer O_3 (reducing TCO) and O_3 precursors including H_2O and OH. The observed positive anomalies in TCO in the western Pacific during El Niño are consistent with suppressed convection and less destruction of O_3 while negative anomalies in the eastern Pacific are consistent with enhanced convection.

A simplified technique (discussed in the appendix) was proposed in this study for estimating maps of TCO in the tropics. This promising approach requires only total ozone gridded measurements and utilizes small variability in TCO near the dateline. Monthly-mean TCO computed from this technique was shown to differ on average (over 1979-1998) by only 2-4 DU from direct CCD-derived TCO. This simplified technique has an obvious advantage compared to the CCD method because the latter requires high-resolution footprint measurements of both reflectivity and total ozone in the presence of tropopause-level cloud tops. We note that the method may also be extended to generate TCO distributions in the tropics on time scales shorter than one month shown in this study.

Appendix: A Simplified Method For Deriving Tropical Tropospheric O_3

This study introduces a simplified method for estimating TCO maps in the tropics. This approach makes use of the small variability observed in TCO near the dateline along with the approximately zonally invariant nature of stratospheric column O_3 (SCO).

Because variability in TCO near the dateline is mostly a weak seasonal cycle, SCO is first derived near the dateline at some chosen reference longitude by subtracting values of CCD TCO $\alpha(t)$ in (1) from total column ozone Ω:

$$SCO(\lambda_0, \phi, t) = \Omega(\lambda_0, \phi, t) - \alpha(\lambda_0, \phi, t). \qquad (A1)$$

In $(A1)$, λ is the longitude (λ_0 is reference longitude), ϕ is latitude, and t represents the month. Reference longitude λ_0 was taken to be 167.5°E which lies near the center of the observed inflection region in CCD ENSO variability (see Figure 7, bottom). From $(A1)$ we next assume to first approximation (as with the CCD method) that for monthly means SCO is zonally invariant and hence the same at all longitudes λ. We note that QBO variability in this region (Figure 7, top) represents comparatively small anomalies (~1-2 DU) and may be neglected as a simplifying approximation.

Tropospheric column O_3 (TCO) at each grid point is then derived by subtracting zonally-invariant SCO in $(A1)$ from coinciding gridded measurements of $\Omega(\lambda, \phi, t)$:

$$TCO(\lambda, \phi, t) = \Omega(\lambda, \phi, t) - \Omega(\lambda_0, \phi, t) + \alpha(\lambda_0, \phi, t). \qquad (A2)$$

An important property in $(A2)$ is the differencing of the two Ω terms. This means that regardless of whatever satellite instrument (e.g., SBUV, Nimbus 7, EP, etc.) is used for Ω, calibration offsets between different instruments will cancel out.

Figure 14 shows values of $\alpha(t)$ at reference longitude 167.5°E, with meridional coveraged extended to ±17.5°. Tables 3 and 4 list the values plotted in Figure 14 and

their 2σ uncertainties. Hence, given only total ozone gridded measurements in the tropics, TCO can be estimated by simply combining ($A2$) with the values shown in Table 3 for $\alpha(t)$. Values in Table 3 may be interpolated to generate ozone maps for time averages shorter than one month used in this study.

In conclusion we mention that differences between TCO derived from the CCD method and this simplified approach are independent of longitude. This follows because stratospheric column amounts for both methods are assumed to be zonally invariant. The RMS differences plotted in Figure 13 for 10°S must therefore be equivalent for all three time series shown.

Acknowledgments. We appreciate greatly the efforts of members of NOAA and of the UARS and TOMS data processing teams in producing the extensive geophysical data sets used in this study. In addition we also thank P. K. Bhartia for important comments and suggestions.

References

Brasseur, G. P., J. T. Kiehl, J.-F. Müller, T. Schneider, C. Granier, X. Tie, Didier Hauglustaine, Past and future changes in global tropospheric ozone: Impact on radiative forcing, *Geophys. Res. Lett., 25*, 3807-3810, 1998.

Chandra, S., J. R. Ziemke, W. Min, and W. G. Read, Effects of 1997-1998 El Niño on tropospheric ozone and water vapor, *Geophys. Res. Lett., 25*, 3867–3870, 1998.

Chandra S., J. R. Ziemke, and R. W. Stewart, An 11-year solar cycle in tropospheric ozone from TOMS measurements, *Geophys. Res. Lett.*, in press, 1999.

Crutzen, P. J, and M. O. Andreae, Biomass burning in the tropics: impact on atmospheric chemistry and biogeochemical cycle, *Science, 250*, 1669–1678, 1990.

Fishman, J., and J. C. Larsen, Distribution of total ozone and stratospheric ozone in the tropics: Implications for the distribution of tropospheric ozone, *J. Geophys. Res., 92*, 6627–6634, 1987.

Fishman, J., C. E. Watson, J. C. Larsen, and J. A. Logan, Distribution of tropospheric ozone determined from satellite data, *J. Geophys. Res., 95*, 3599–3617, 1990.

Fishman, J., K. Fakhruzzaman, B. Cros, and D. Nganga, Identification of widespread pollution in the southern hemisphere deduced from satellite analyses, *Science, 252*, 1693–1696, 1991.

Fishman, J., V. G. Brackett, and K. Fakhruzzaman, Distribution of tropospheric ozone in the tropics from satellite and ozonesonde measurements, *J. Atmos. Terr. Phys., 54*, 589–597, 1992.

Fishman, J., V. G. Brackett, E. V. Browell, and W. B. Grant, Tropospheric ozone derived from TOMS/SBUV measurements during TRACE A, *J. Geophys. Res., 101*, 24,069–24,082, 1996.

Gage, K., S., and G. C. Reid, Longitudinal variations in tropical tropopause properties in relation to tropical convection and El Niño-Southern Oscillation events, *J. Geophys. Res., 92*, 14,197–14,203, 1987.

Haigh, J. D., The impact of solar variability on climate, *Science, 272*, 981-984, 1996.

Hansen, J., M. Sato, and R. Ruedy, Radiative forcing and climate response, *J. Geophys. Res., 102*, 6831–6864, 1997.

Herman, J. R., P. K. Bhartia, O. Torres, N. C. Hsu, C. J. Seftor, and E. Celerier, Global distribution of absorbing aerosols from Nimbus-7/TOMS data, *J. Geophys. Res., 102*, 16,911-16,922, 1997.

Hsu, N. C., J.R. Herman, P.K. Bhartia, C.J. Seftor, O. Torres, A.M. Thompson, J.F. Gleason, T.F. Eck, and B.N. Holben, Detection of biomass burning smoke from TOMS measurements, *Geophy. Res. Let. 23*, 745–748, 1996.

Hudson, R. D., and A. M. Thompson, Tropical tropospheric ozone (TTO) from TOMS by a modified-residual method, *J. Geophys. Res. 103*, 22,129–22,145, 1998.

Jacob, J., et al., Origin of ozone and NO_x in the tropical troposphere: A photochemical analysis of aircraft observations over the South Atlantic basin, *J. Geophys. Res., 101*, 24,235–24,250, 1996.

Komala, N., S. Saraspriya, K. Kita, and T. Ogawa, Tropospheric ozone behavior observed in Indonesia, *Atmos. Environ., 30*, 1851–1856, 1996.

Krishnamurti, T. N, H. E. Fuelberg, M. C. Sinha, D. Oosterhof, E. L. Bensman, and V. B. Kumar, The meteorological environment of the tropospheric ozone maximum over the tropical South Atlantic Ocean, *J. Geophys. Res., 98*, 10,621–10,641, 1993.

Krishnamurti, T. N., M. C. Sinha, M. Kanamitsu, D. Oosterhof, H. Fuelberg, R. Chatfield, D. J. Jacob, and J. Logan, Passive tracer transports relevant to the TRACE A Experiment, *J. Geophys. Res., 101*, 23,889–23,907, 1996.

Liebmann, B., and C. A. Smith, Description of a complete (interpolated) outgoing longwave radiation dataset, *Bull. Am. Meteorol. Soc., 77*, 1275–1277, 1996.

Logan, J. A., An analysis of ozonesonde data for the troposphere: Recommendations for testing 3-D models, and development of a gridded climatology for tropospheric ozone, *J. Geophys. Res.*, submitted, 1998.

Randel, W. J., and J. B. Cobb, Coherent variations of monthly mean total ozone and lower stratospheric temperature, *J. Geophys. Res., 99*, 5433–5447, 1994.

Randel, W. J., F. Wu, J. M. Russell III, J. W. Waters, and L. Froidevaux, Ozone and

temperature changes in the stratosphere following the eruption of Mount Pinatubo, *J. Geophys. Res., 100*, 16,753–16,764, 1995.

Thompson, A. M., K. E. Pickering, D. P. McNamara, M. R. Schoeberl, R. D. Hudson, J. H. Kim, E. V. Browell, V. W. J. H. Kirchhoff, and D. Nganga, Where did tropospheric ozone over southern Africa and the tropical Atlantic come from in October 1992? Insights from TOMS, GTE/TRACE-A and SAFARI-92, *J. Geophys. Res., 101*, 24,251–24,278, 1996.

Wallace, J. M., R. L. Panetta, and J. Estberg, Representation of the equatorial stratospheric quasi-biennial oscillation in EOF phase space, *J. Atmos. Sci., 50*, 1751–1762, 1993.

Wang, Y., D. J. Jacob, and J. A. Logan, Global simulation of tropospheric $O_3 - NO_x$-hydrocarbon chemistry, 1, Model formulation, *J. Geophys. Res., 103*, 10,713–10,726, 1998a.

Wang, Y., D. J. Jacob, J. A. Logan, Global simulation of tropospheric $O_3 - NO_x$-hydrocarbon chemistry, 3, Origin of tropospheric ozone and effects of nonmethane hydrocarbons, *J. Geophys. Res., 103*, 10,757–10,768, 1998b.

Watson, C. E., J. Fishman, and H. G. Reichle Jr., The significance of biomass burning as a source of carbon monoxide and ozone in the southern hemisphere tropics: A satellite analysis, *J. Geophys. Res., 95*, 16,443–16,450, 1990.

Ziemke, J. R., S. Chandra, A. M. Thompson, and D. P. McNamara, Zonal asymmetries in southern hemisphere column ozone: Implications of biomass burning, *J. Geophys. Res., 101*, 14,421–14,427, 1996.

Ziemke, J. R., S. Chandra, R. D. McPeters, and P. A. Newman, Dynamical proxies of column ozone with applications to global trend models, *J. Geophys. Res., 102*, 6117–6129, 1997.

Ziemke, J. R., and S. Chandra, On tropospheric ozone and the tropical wave 1 in total column ozone, *Proc. 18th Quadrenn. Ozone Symp., 1*, 447–450, 1998.

Ziemke, J. R., S. Chandra, P. K. Bhartia, Two new methods for deriving tropospheric column ozone from TOMS measurements: The assimilated UARS MLS/HALOE and

convective-cloud differential techniques, *J. Geophys. Res.*, *103*, 22,115–22,127, 1998.

This manuscript was prepared with the AGU LaTeX macros v3.1.

Figure 1. Column ozone (Dobson units) plotted versus longitude for Earth Probe TOMS (dotted) and 0-100 hPa UARS HALOE (solid) during El Niño (top frames, September 12, 1997 and October 17, 1997) and non-El Niño (bottom frames, June 28, 1998 and July 4, 1998) conditions. Earth Probe TOMS total column values were derived from the averaging of 4-point nearest-neighbor 1°× 1.25°gridded level-3 data coincident with HALOE latitude-longitude locations. (Latitudes for HALOE lie between 10°S and 10°N.) For Earth Probe TOMS total column ozone, 30 Dobson units were subtracted to better visual comparison with HALOE column amounts.

Figure 2. Monthly-mean tropospheric column O_3 time series from the CCD method (solid) plotted with coincident ground-based ozonesonde measurements (dotted) at Samoa (14°S, 170°W) and Nairobi (1°S, 37°E). The CCD time at Nairobi used EP TOMS measurements and had 5 DU subtracted relative to Nimbus 7 to account for instrumental bias (discussed in section 3). Uncertainty bars for sonde measurements represent $\pm 1\sigma$ temporal standard devidations. Measurement uncertainty bars for the CCD measurements (upper right in each frame) represent $\pm 2\sigma$ standard deviations.

Figure 3. Tropospheric column O_3 time series along the equator from the CCD data (dark) and regression model (light, see section 2). (left) Equator, 145°W-150°W in the eastern Pacific. (middle) Equator, 5°W-5°E in the central Atlantic. (right) Equator, 110°E-115°E in the western Pacific. All time series were derived by averaging data at 2.5°S and 2.5°N and include a 3-month running average for plotting. Mean RMS differences between CCD and model time series for these three locations are 2.5, 3.4, and 2.3 DU, respectively.

Figure 4. Seasonal cycles $\alpha(t)$ in column O_3 derived from the regression model (see section 2) for total column O_3 (light solid), stratospheric column O_3 (dotted), and tropospheric column O_3 (dark solid) at six tropical locations (indicated). For better visual comparison with tropospheric column O_3 results, 190 DU (175 DU) was subtracted from total column O_3 (stratospheric column O_3).

Figure 5. Mean seasonal cycles (in Dobson units) in TCO at Hilo (20°N, 155°W) for ozonesonde (dotted) and CCD (solid) measurements. Sonde and CCD TCO climatologies were derived using all available data between 1982 and 1992. The sonde data included 375 ozone and temperature profiles. Vertical bars represent $\pm 1\sigma$ temporal standard deviations.

Figure 6. Latitude versus longitude annual means (top) and annual amplitudes (bottom) of 1979-1992 CCD TCO derived from $\alpha(t)$ in (1). These column amounts are in Dobson units.

Figure 7. Latitude versus longitude tropospheric column O_3 QBO coefficients (top, in Dobson units per 10 m s^{-1}) and ENSO coefficients (bottom, in Dobson units per unit of $ENSO(t)$) for the same regression model as in Figure 6. Shading indicates regions where coefficients are not different from zero at the 2σ level.

Figure 8. Time series of CCD monthly-mean tropospheric column O_3 (solid) plotted versus stratospheric column O_3 (dotted) along the Equator averaged between 5° W and 5° E. Stratospheric column O_3 was multiplied by the factor 0.5. The tropospheric column O_3 time series was shifted 3 months backward in time for maximum anticorrelation with stratospheric column O_3 (discussed in section 3). A 3-month running average was applied to both time series for plotting.

Figure 9. (top) Time series of CCD monthly-mean tropospheric column O_3 (solid) plotted versus concurrent NOAA OLR (dotted) along the Equator averaged between 5° W and 5° E. (bottom) The same CCD time series (solid) plotted versus concurrent TOMS aerosol-smoke index data (dashed). Both OLR and aerosol index time series have been rescaled (indicated) in each case. All time series include a 3-month running average for plotting.

Figure 10. (top) Time series of CCD monthly-mean tropospheric column O_3 (solid) plotted versus concurrent NOAA OLR (dotted) along the Equator in the western Pacific at longitude 117.5° E. (bottom) Time series of CCD monthly-mean tropospheric column O_3 (solid) plotted versus concurrent NOAA OLR (dotted) along the Equator in the eastern Pacific at longitude 147.5° W. All time series include a 3-month running average for plotting.

Figure 11. Tropospheric column ozone (Dobson units) in the tropics derived from the CCD method. (top) October 1996. (bottom) October 1997.

Figure 12. (top) Time series of CCD monthly-mean tropospheric column O_3 (solid) plotted versus concurrent NOAA OLR (dotted) averaged over 10° S-10° N and 90° E-150° E. (bottom) The same time series of CCD monthly-mean tropospheric column O_3 (solid) plotted versus concurrent TOMS aerosol-smoke index data (dashed). Both OLR and aerosol index time series have been rescaled (indicated) in each case. All time series include a 3-month running average for plotting.

Figure 13. Tropospheric column O_3 time series at 10° S from the CCD method (dark) and simplified method (light, see appendix). (left) 10° S, 145°W-150°W in the eastern Pacific. (middle) 10° S, 5°W-5°E in the central Atlantic. (right) 10° S, 110°E-115°E in the western Pacific. These time series along 10° S were generated by averaging data at 12.5°S and 7.5°S. The simplified method includes total ozone data from NOAA SBUV2 for May 1993-December 1994 to help fill in data between the demise of Nimbus 7 TOMS and the beginning of Earth Probe TOMS. Plotted along the bottom of each frame are absolute value differences between CCD and the simplified method. The 1979-1998 mean RMS difference between CCD and the simplified method is 2.7 DU for these data at 10°S. Mean RMS differences for data at orginal latitudes 12.5°S, 7.5°S, 2.5°S, 2.5°N, 7.5°N, and 12.5°N are 3.8, 3.6, 3.3, 2.9, 3.6, and 3.6 DU, respectively.

Figure 14. Nimbus 7 TOMS 1979-1992 CCD seasonal fit $\alpha(t)$ (in Dobson units) along longitude 167.5° E (see section 2). Contour interval is 1 Dobson unit.

Table 1. Seasonally-averaged Tropopause Pressure (hPa), Tropopause Height (km), Tropospheric Column Ozone (DU), and Number of Profiles[a] Derived From Available 1978-1996 Tropical Ozonesonde Measurements

Station	Dec.-Feb.	March-May	June-Aug.	Sept.-Nov.
Ascension (8°S, 15°W)	91, 17.4, 41, (17)	95, 17.0, 31, (16)	106, 16.4, 45, (7)	95, 17.1, 46, (26)
Natal (5°S, 35°W)	94, 16.9, 36, (46)	95, 16.9, 27, (48)	104, 16.4, 37, (54)	102, 16.5, 43, (85)
Brazzaville (4°S, 15°E)	104, 16.5, 41, (14)	104, 16.4, 34, (11)	93, 17.1, 41, (22)	102, 16.6, 43, (34)
Samoa (14°S, 170°W)	92, 17.2, 24, (30)	94, 17.1, 21, (31)	98, 16.8, 25, (45)	100, 16.8, 27, (51)

[a]Total number of profiles averaged per season are shown in parentheses

Table 2. Variance[a] Explained by Individual Terms in (1)

Location	$\Omega(t)$	$\alpha(t)$	βt	γ QBO(t)	δ solar(t)	ϵ ENSO(t)	R(t)
Equator, 112.5E	7.53(100)	1.92(25.5)	0.31(4.10)	0.16(2.06)	0.15(2.00)	3.04(40.4)	2.48(32.9)
Equator, 0E	9.41(100)	4.10(46.8)	0.20(2.08)	0.82(8.75)	0.56(5.99)	0.68(7.23)	3.43(36.4)
Equator, 147.5W	6.33(100)	0.32(4.98)	0.22(3.40)	0.27(4.21)	0.78(12.3)	3.05(48.2)	2.25(35.6)

[a]Numbers in parentheses are in units percent of total variance. All other numbers are in DU^2.

Table 3. CCD 1979-1992 Seasonal Fit Tropospheric Column O_3[a] at 167.5°E

Latitude	Jan.	Feb.	March	April	May	June	July	Aug.	Sept.	Oct.	Nov.	Dec.
17.5°	16.7	17.4	22.7	28.4	30.0	27.3	23.8	23.5	26.1	28.0	26.1	20.9
12.5°	19.9	21.7	26.9	31.2	30.9	26.2	21.2	20.0	22.6	25.6	25.3	22.2
7.5°	21.6	23.0	25.7	27.3	25.9	22.3	19.2	18.7	20.6	22.8	23.2	22.2
2.5°	21.7	22.6	23.1	22.4	20.8	19.0	18.1	18.1	18.9	19.7	20.2	20.8
-2.5°	22.1	21.7	21.0	20.3	19.9	19.7	19.8	20.0	20.3	20.9	21.5	22.0
-7.5°	23.8	22.6	21.8	21.6	21.7	21.7	21.6	21.9	22.7	24.0	24.9	24.8
-12.5°	25.6	23.2	22.3	23.0	23.9	24.1	23.7	24.0	25.7	27.9	29.1	28.1
-17.5°	27.5	25.1	24.9	25.5	24.6	21.8	19.5	20.4	24.8	29.9	32.4	31.0

[a]Numbers are in Dobson Units

Table 4. CCD 1979-1992 Seasonal Fit Tropospheric Column O_3 2σ[a] at 167.5°E

Latitude	Jan.	Feb.	March	April	May	June	July	Aug.	Sept.	Oct.	Nov.	Dec.
17.5°	3.4	4.4	4.6	5.4	3.4	2.5	1.8	1.2	1.3	1.6	2.3	3.7
12.5°	2.6	3.1	2.9	2.5	2.0	1.4	1.1	1.0	1.3	1.6	1.7	2.0
7.5°	1.2	2.2	1.4	1.6	1.6	1.1	0.9	0.9	1.1	1.5	1.1	1.6
2.5°	0.8	1.3	1.4	1.5	1.3	0.7	0.7	1.3	1.6	1.1	1.2	0.9
-2.5°	1.1	1.7	1.3	1.4	0.9	0.8	0.9	1.5	1.7	0.9	1.6	1.0
-7.5°	1.2	1.5	1.7	1.0	1.4	1.0	1.2	1.4	1.4	1.8	1.9	1.2
-12.5°	0.8	1.0	1.4	1.1	1.1	1.5	1.3	2.4	1.7	2.5	2.1	1.8
-17.5°	1.3	1.4	1.7	1.2	2.0	2.2	2.2	4.2	3.0	2.7	2.1	2.0

[a]Numbers are in Dobson Units

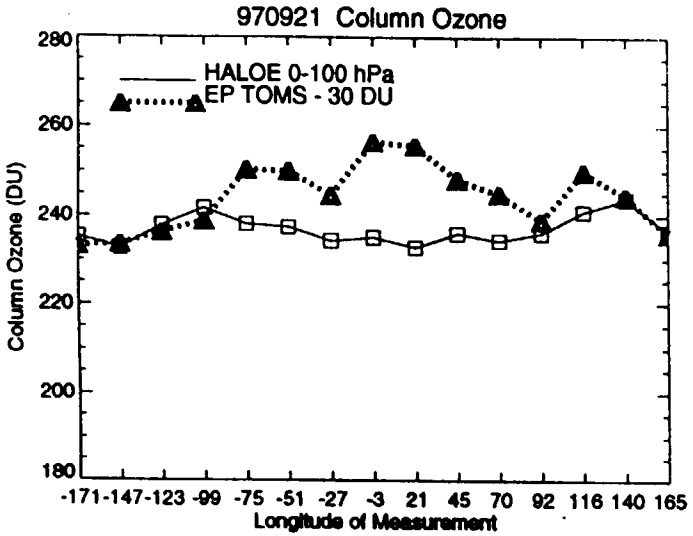
970921 Column Ozone
HALOE 0-100 hPa
EP TOMS - 30 DU
Column Ozone (DU)
280
260
240
220
200
180
-171 -147 -123 -99 -75 -51 -27 -3 21 45 70 92 116 140 165
Longitude of Measurement

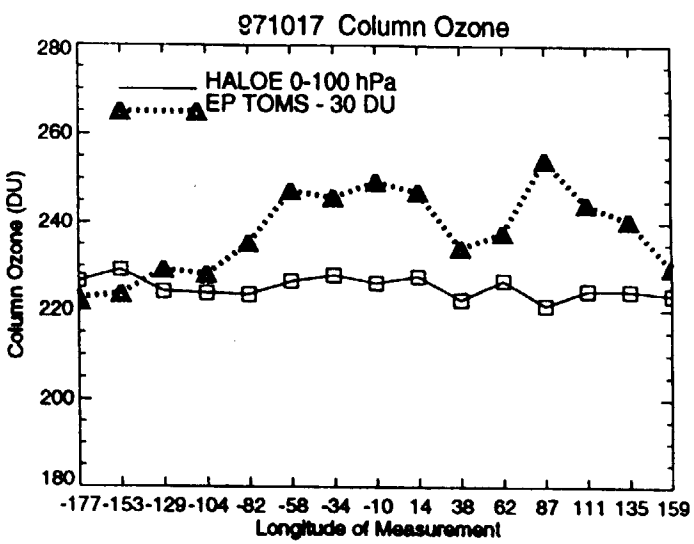
971017 Column Ozone
HALOE 0-100 hPa
EP TOMS - 30 DU
Column Ozone (DU)
280
260
240
220
200
180
-177 -153 -129 -104 -82 -58 -34 -10 14 38 62 87 111 135 159
Longitude of Measurement

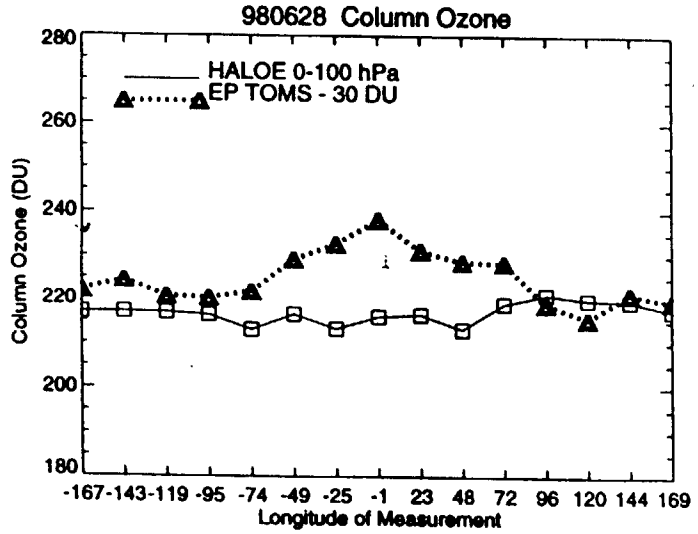
980628 Column Ozone
HALOE 0-100 hPa
EP TOMS - 30 DU
Column Ozone (DU)
280
260
240
220
200
180
-167 -143 -119 -95 -74 -49 -25 -1 23 48 72 96 120 144 169
Longitude of Measurement

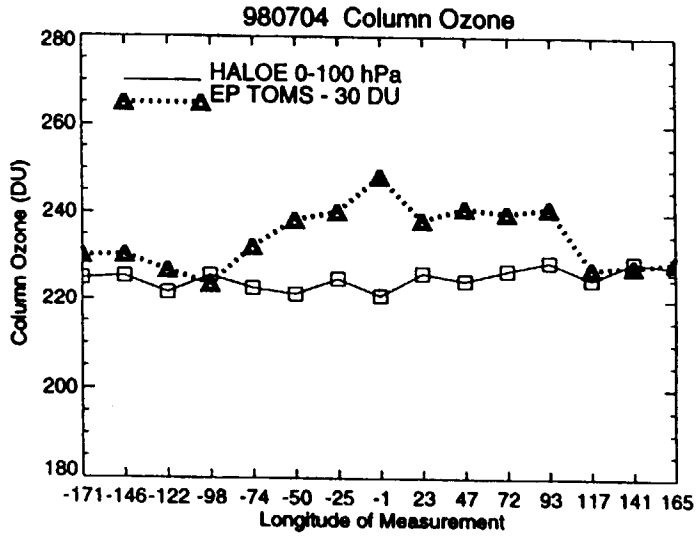
980704 Column Ozone
HALOE 0-100 hPa
EP TOMS - 30 DU
Column Ozone (DU)
280
260
240
220
200
180
-171 -146 -122 -98 -74 -50 -25 -1 23 47 72 93 117 141 165
Longitude of Measurement

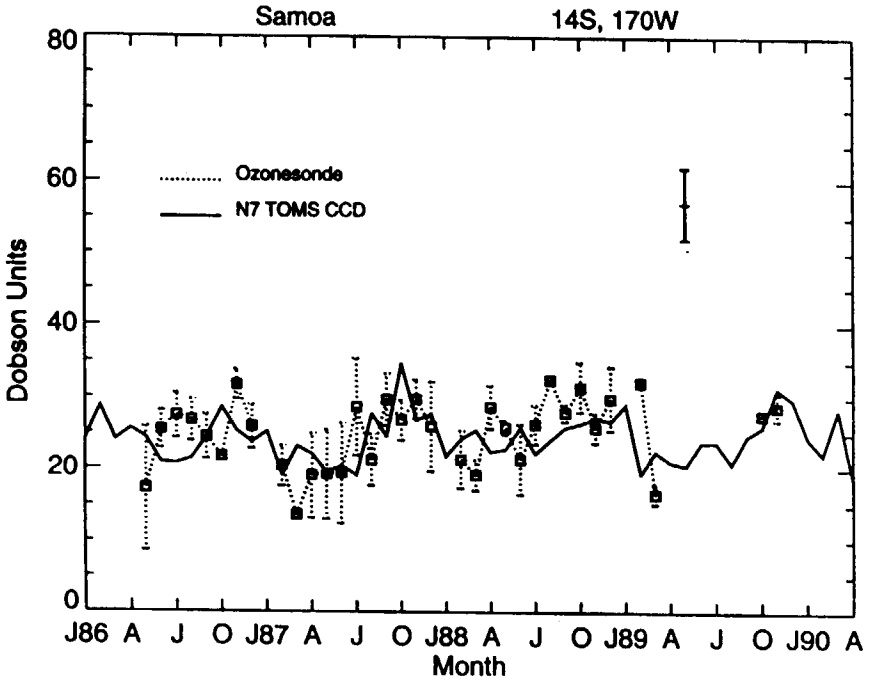
Samoa
14S, 170W
Ozonesonde
N7 TOMS CCD
Dobson Units
0
20
40
60
80
J86 A J O J87 A J O J88 A J O J89 A J O J90 A
Month

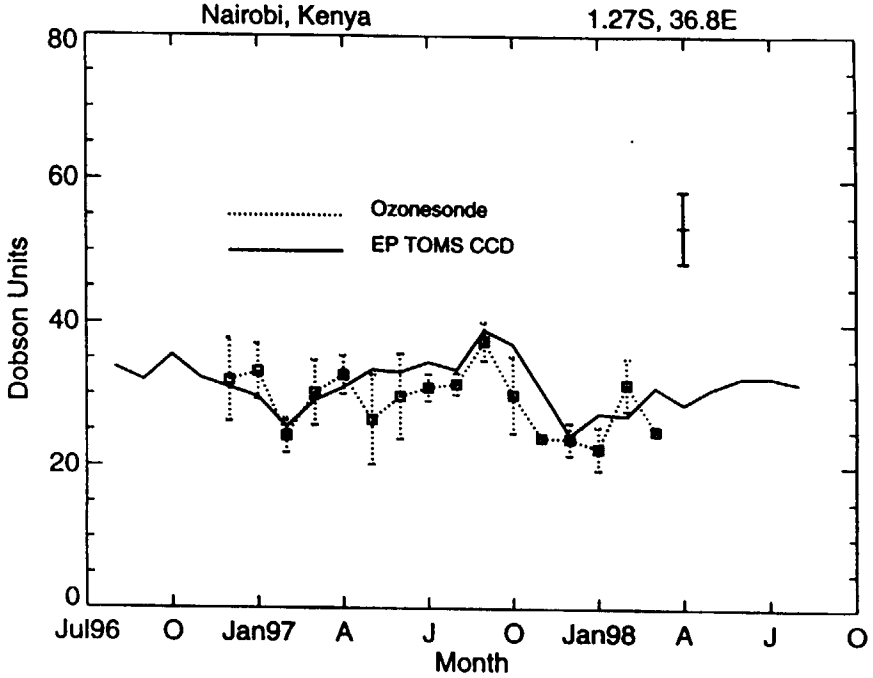
Nairobi, Kenya
1.27S, 36.8E
Ozonesonde
EP TOMS CCD
Dobson Units
0
20
40
60
80
Jul96 O Jan97 A J O Jan98 A J O
Month

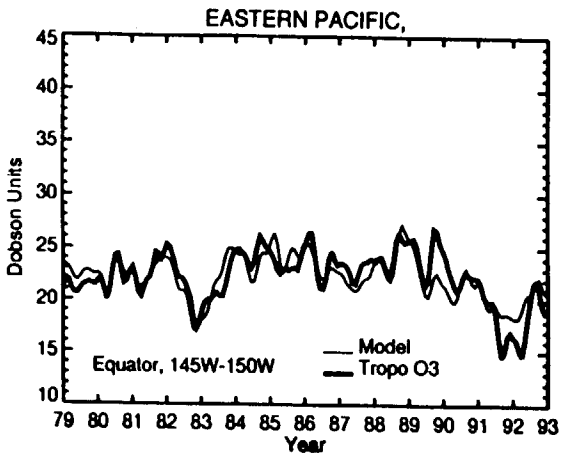
EASTERN PACIFIC,
Dobson Units
45
40
35
30
25
20
15
10
79 80 81 82 83 84 85 86 87 88 89 90 91 92 93
Year
Equator, 145W-150W
Model
Tropo O3

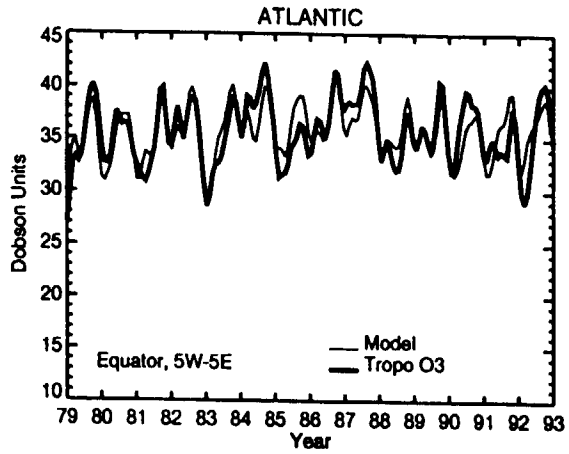
ATLANTIC
Dobson Units
45
40
35
30
25
20
15
10
79 80 81 82 83 84 85 86 87 88 89 90 91 92 93
Year
Equator, 5W-5E
Model
Tropo O3

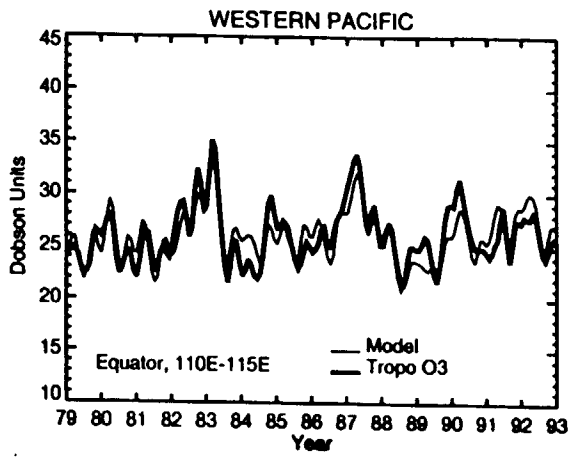
WESTERN PACIFIC
Dobson Units
45
40
35
30
25
20
15
10
79 80 81 82 83 84 85 86 87 88 89 90 91 92 93
Year
Equator, 110E-115E
Model
Tropo O3

w

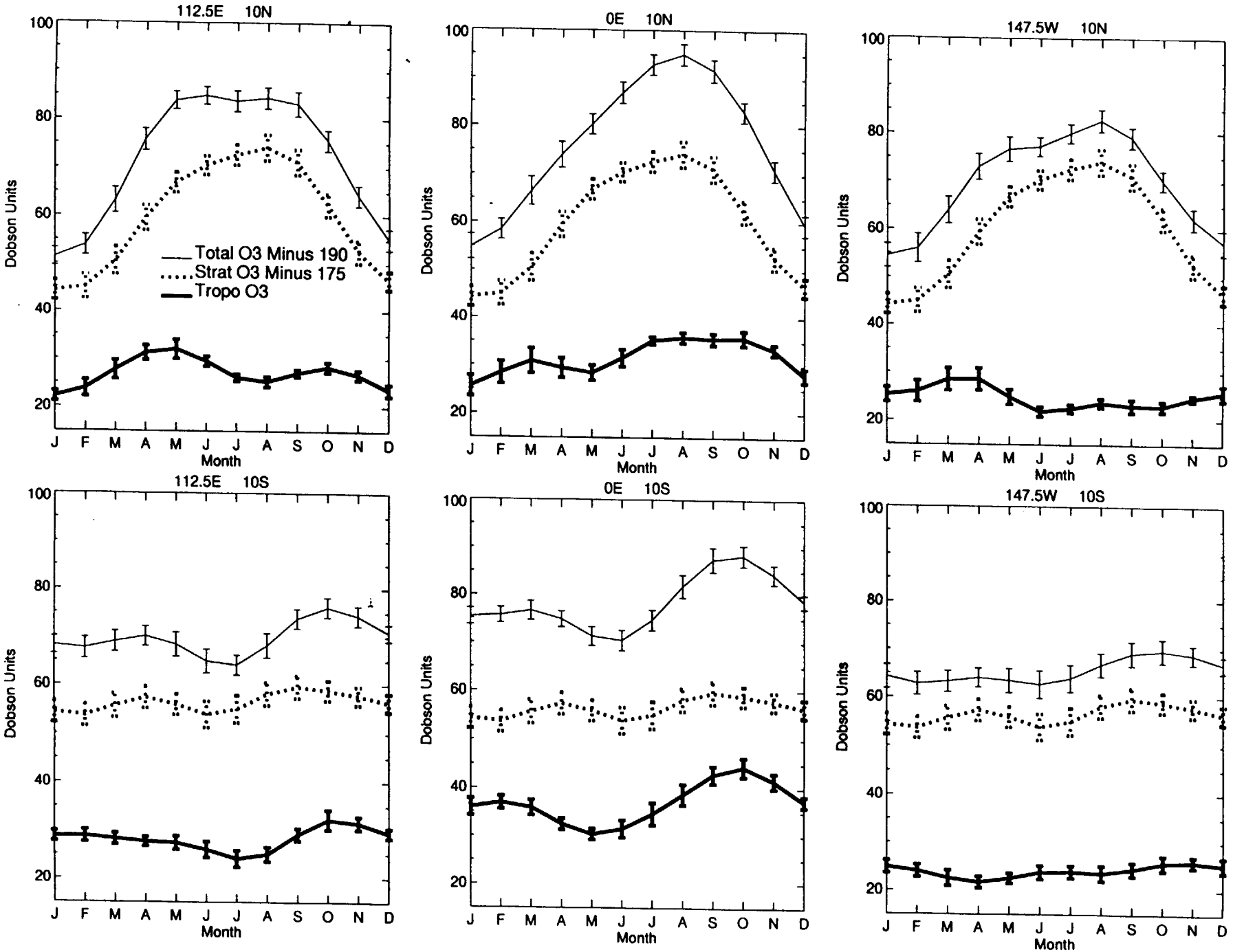
112.5E 10N
0E 10N
147.5W 10N
112.5E 10S
0E 10S
147.5W 10S
Total O3 Minus 190
Strat O3 Minus 175
Tropo O3
Dobson Units
Month
J F M A M J J A S O N D
20
40
60
80
100

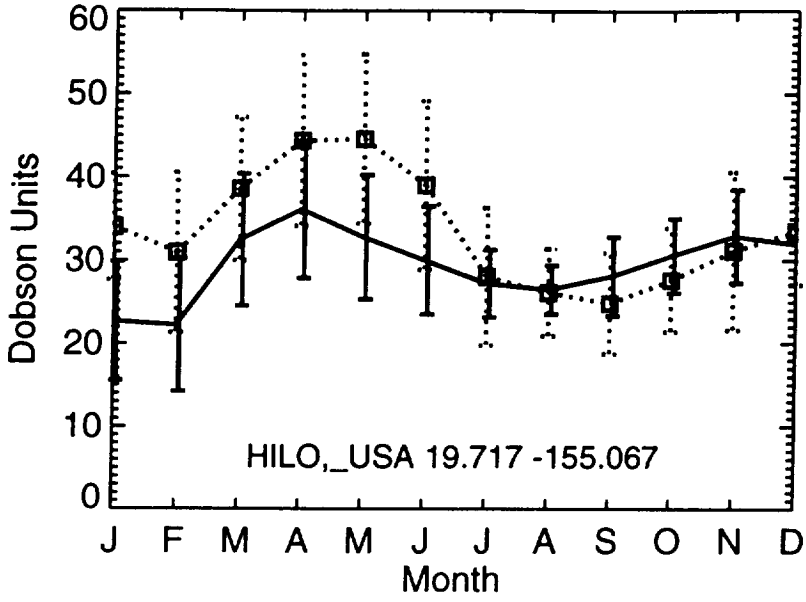
60
50
40
30
20
10
0
Dobson Units
HILO,_USA 19.717 -155.067
J F M A M J J A S O N D
Month

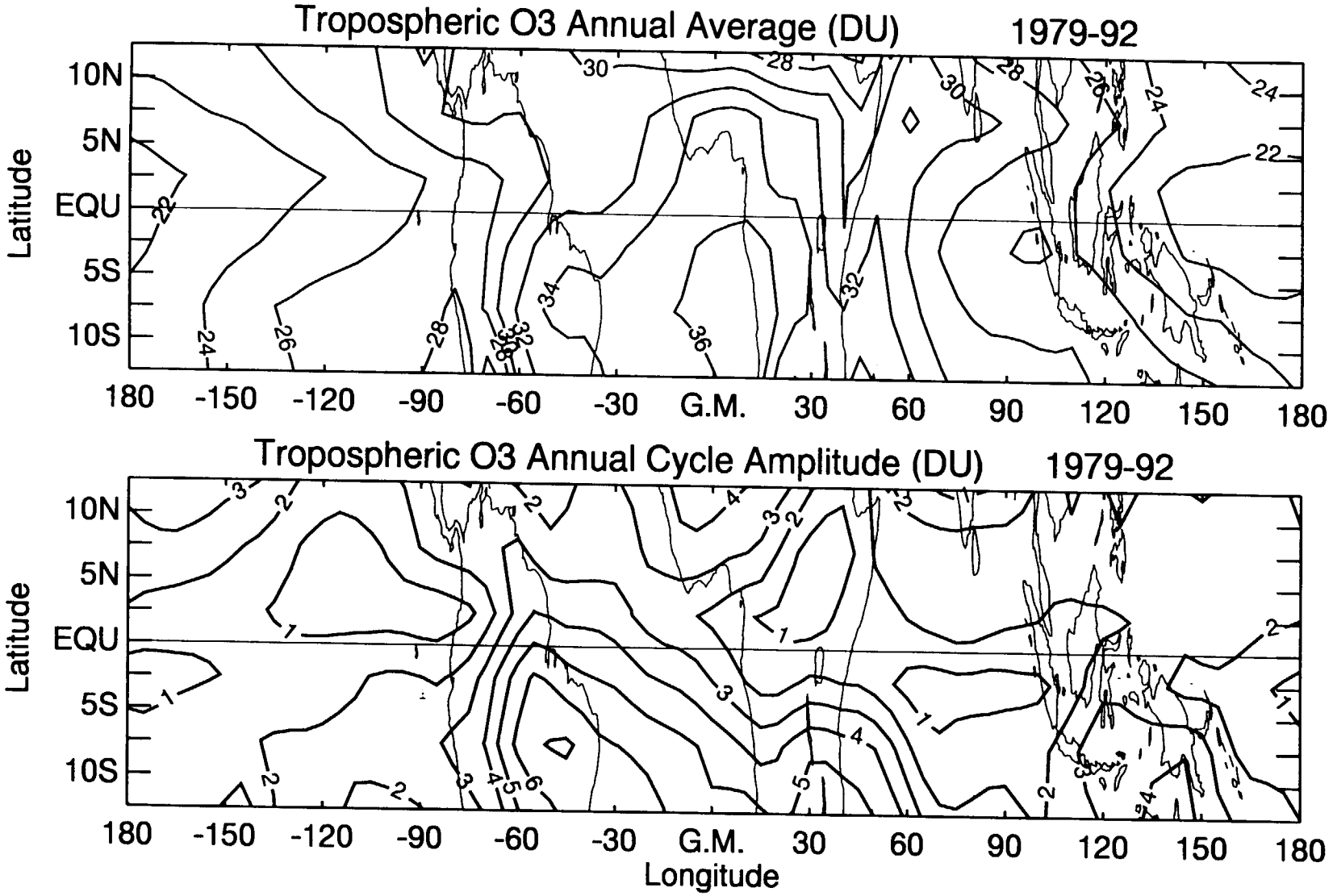
Tropospheric O3 Annual Average (DU) 1979-92
10N
5N
EQU
5S
10S
Latitude
180 -150 -120 -90 -60 -30 G.M. 30 60 90 120 150 180
Tropospheric O3 Annual Cycle Amplitude (DU) 1979-92
10N
5N
EQU
5S
10S
Latitude
180 -150 -120 -90 -60 -30 G.M. 30 60 90 120 150 180
Longitude

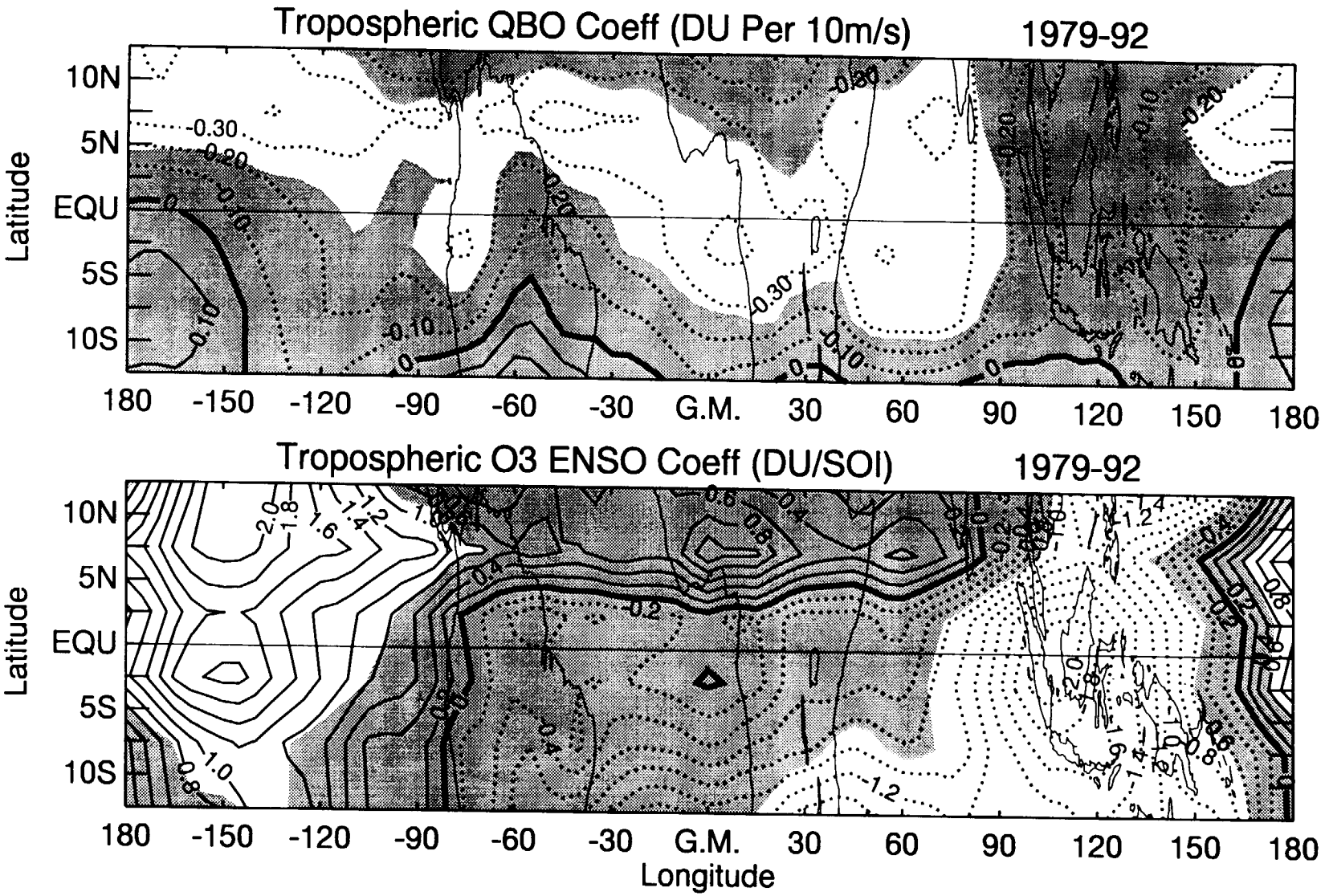
Tropospheric QBO Coeff (DU Per 10m/s) 1979-92
Latitude
10N
5N
EQU
5S
10S
180 -150 -120 -90 -60 -30 G.M. 30 60 90 120 150 180
Tropospheric O3 ENSO Coeff (DU/SOI) 1979-92
Latitude
10N
5N
EQU
5S
10S
180 -150 -120 -90 -60 -30 G.M. 30 60 90 120 150 180
Longitude

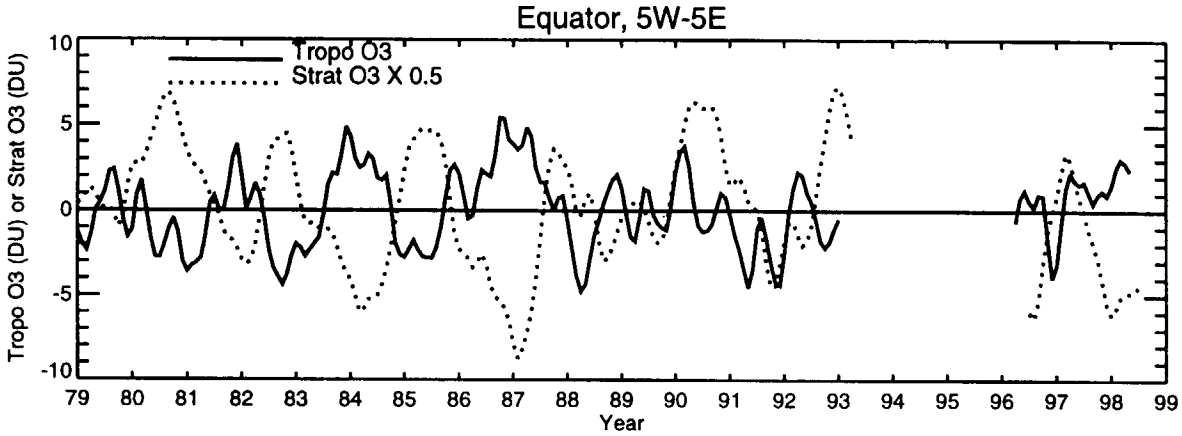
Equator, 5W-5E
Tropo O3
Strat O3 X 0.5
Tropo O3 (DU) or Strat O3 (DU)
10
5
0
-5
-10
79
80
81
82
83
84
85
86
87
88
89
90
91
92
93
94
95
96
97
98
99
Year

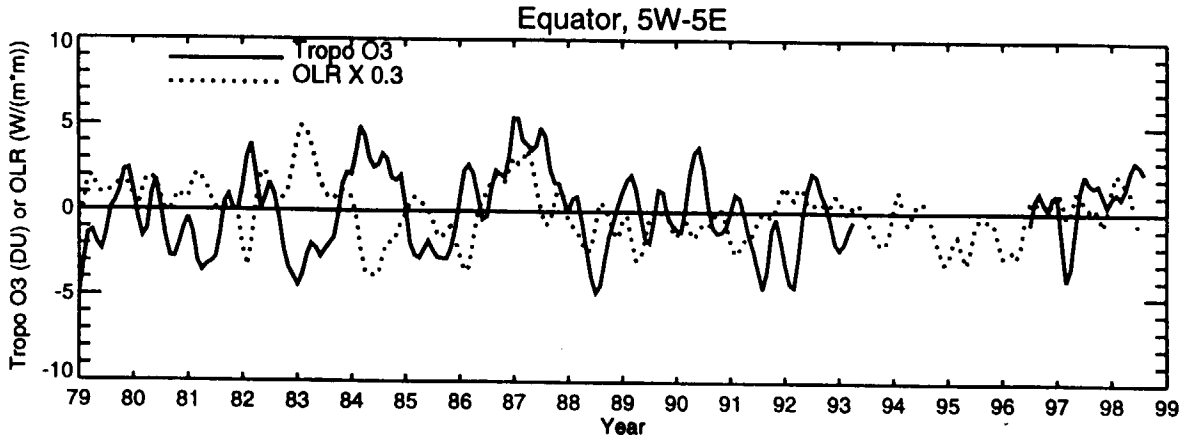
Equator, 5W-5E
Tropo O3
OLR X 0.3
Tropo O3 (DU) or OLR (W/(m*m))
10
5
0
-5
-10
79 80 81 82 83 84 85 86 87 88 89 90 91 92 93 94 95 96 97 98 99
Year

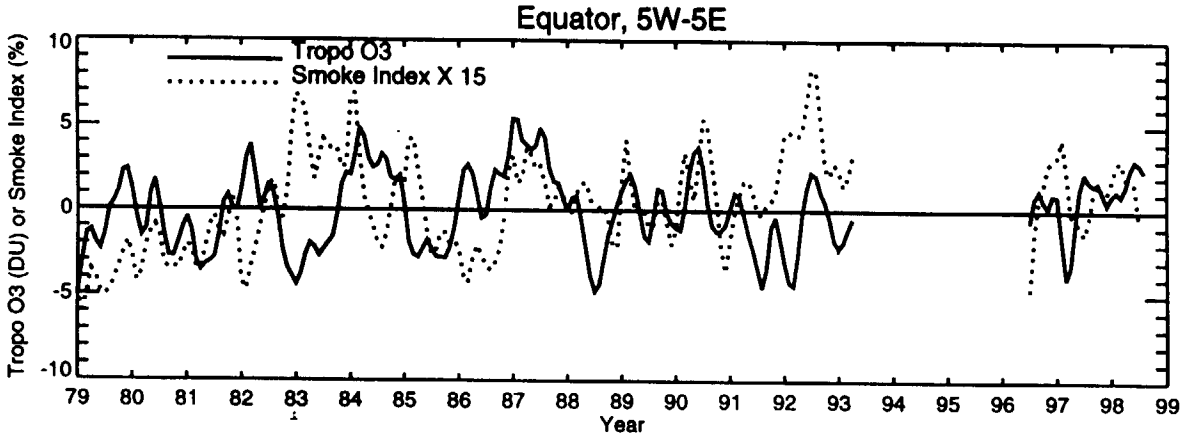
Equator, 5W-5E
Tropo O3
Smoke Index X 15
Tropo O3 (DU) or Smoke Index (%)
10
5
0
-5
-10
79 80 81 82 83 84 85 86 87 88 89 90 91 92 93 94 95 96 97 98 99
Year

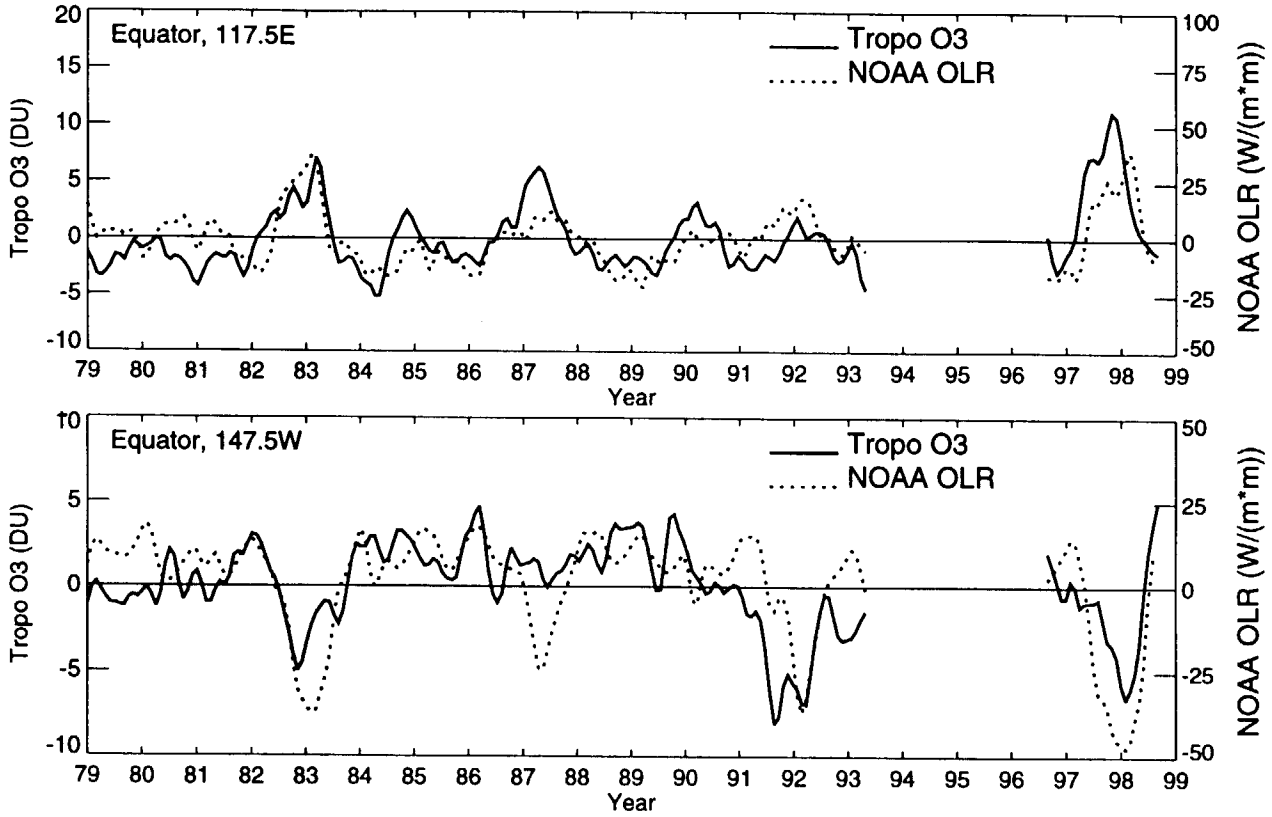
Equator, 117.5E
Tropo O3
NOAA OLR
Tropo O3 (DU)
NOAA OLR (W/(m*m))
Year
Equator, 147.5W
Tropo O3
NOAA OLR
Tropo O3 (DU)
NOAA OLR (W/(m*m))
Year

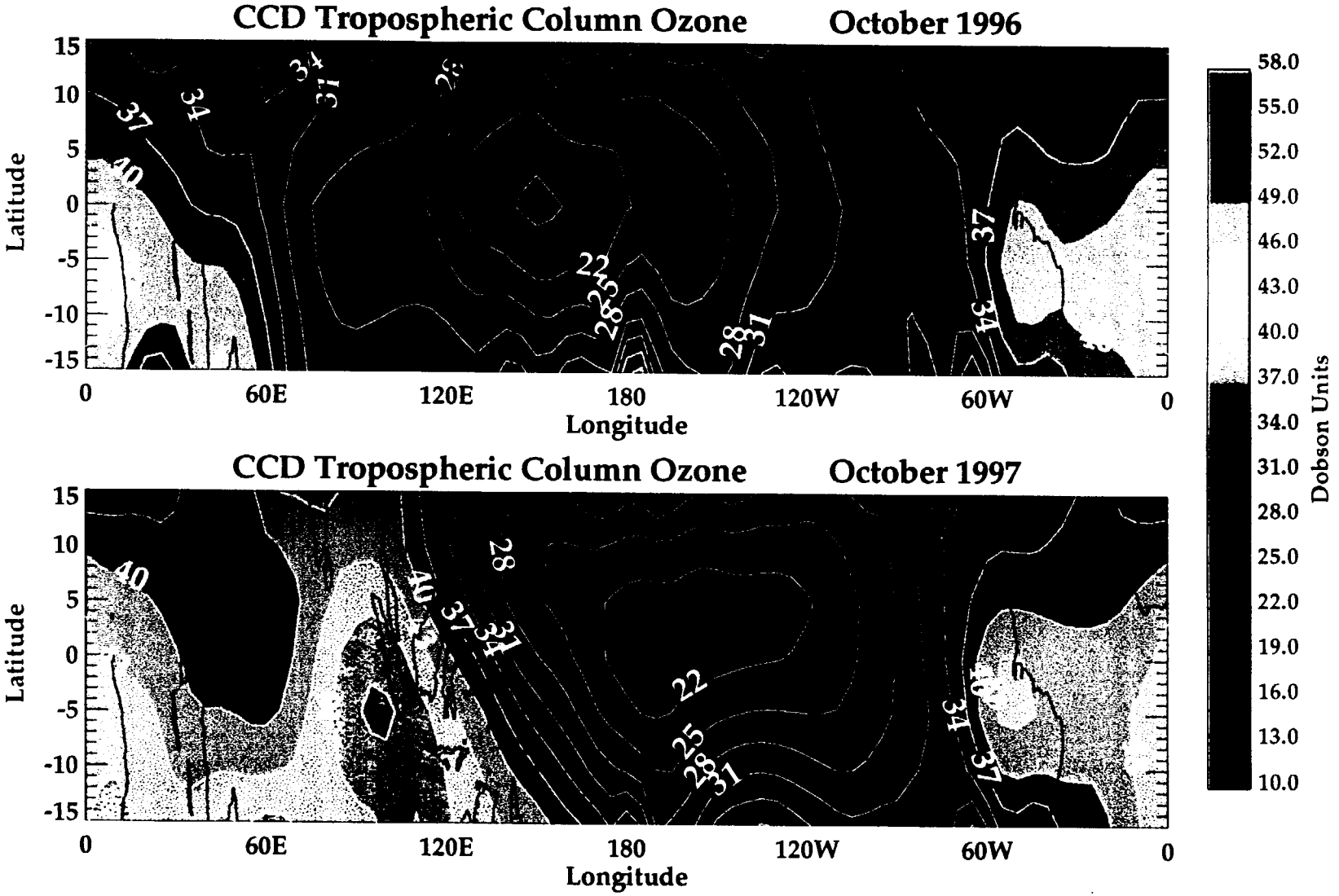
CCD Tropospheric Column Ozone October 1996
CCD Tropospheric Column Ozone October 1997
Latitude
Longitude
15
10
5
0
-5
-10
-15
0
60E
120E
180
120W
60W
0
58.0
55.0
52.0
49.0
46.0
43.0
40.0
37.0
34.0
31.0
28.0
25.0
22.0
19.0
16.0
13.0
10.0
Dobson Units

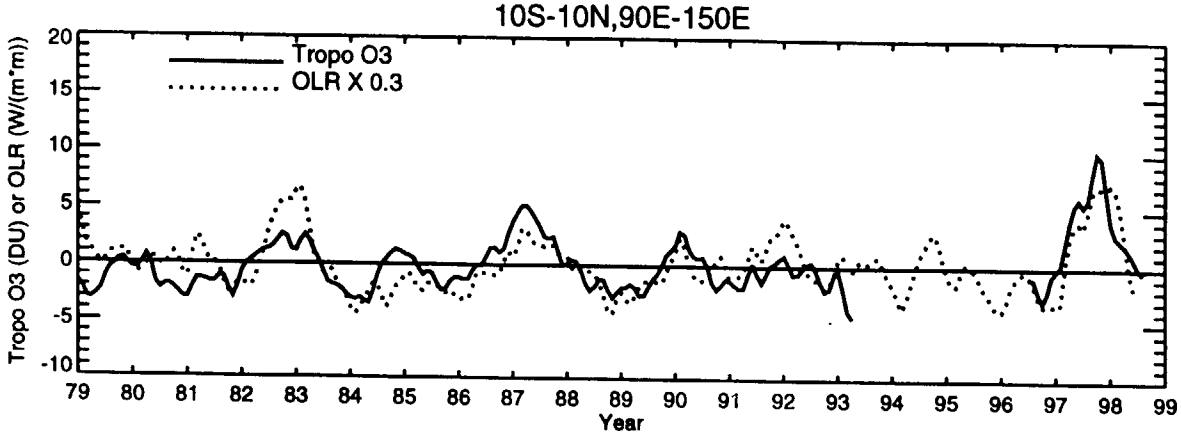
10S-10N,90E-150E
Tropo O3
OLR X 0.3
Tropo O3 (DU) or OLR (W/(m*m))
20
15
10
5
0
-5
-10
79 80 81 82 83 84 85 86 87 88 89 90 91 92 93 94 95 96 97 98 99
Year

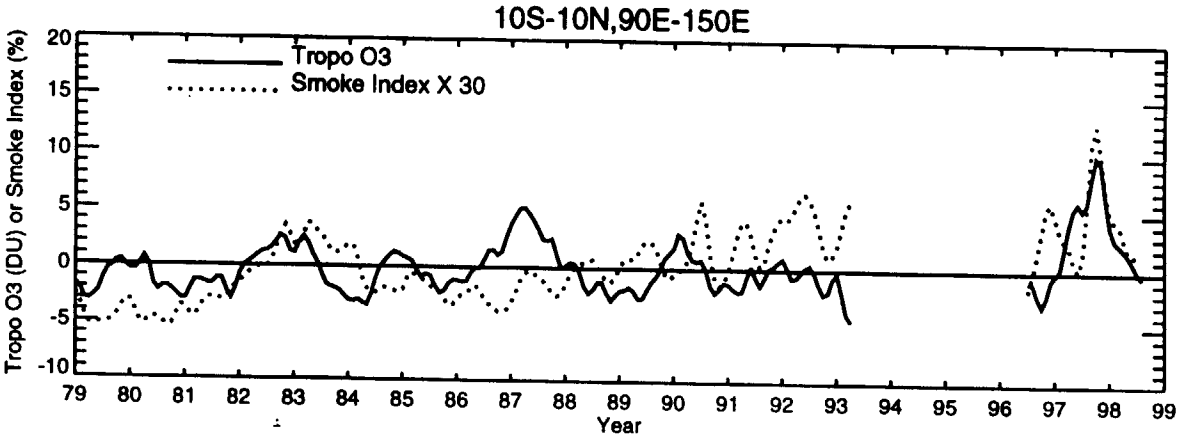
10S-10N,90E-150E
Tropo O3
Smoke Index X 30
Tropo O3 (DU) or Smoke Index (%)
20
15
10
5
0
-5
-10
79 80 81 82 83 84 85 86 87 88 89 90 91 92 93 94 95 96 97 98 99
Year

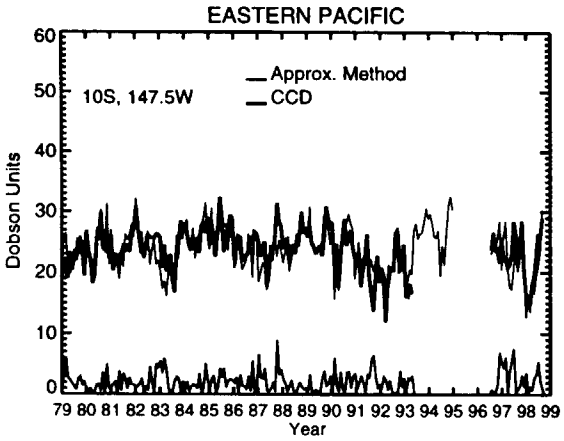
EASTERN PACIFIC
10S, 147.5W
Approx. Method
CCD
Dobson Units
0
10
20
30
40
50
60
79 80 81 82 83 84 85 86 87 88 89 90 91 92 93 94 95 96 97 98 99
Year

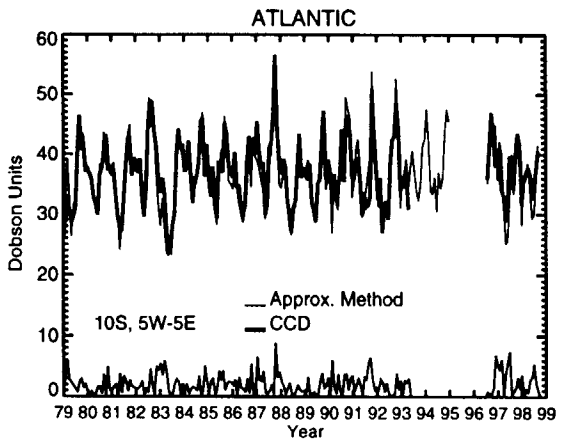
ATLANTIC
10S, 5W-5E
Approx. Method
CCD
Dobson Units
0
10
20
30
40
50
60
79 80 81 82 83 84 85 86 87 88 89 90 91 92 93 94 95 96 97 98 99
Year

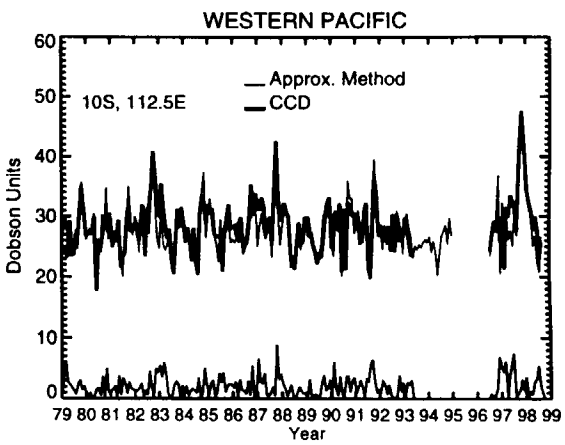
WESTERN PACIFIC
10S, 112.5E
Approx. Method
CCD
Dobson Units
0
10
20
30
40
50
60
79 80 81 82 83 84 85 86 87 88 89 90 91 92 93 94 95 96 97 98 99
Year

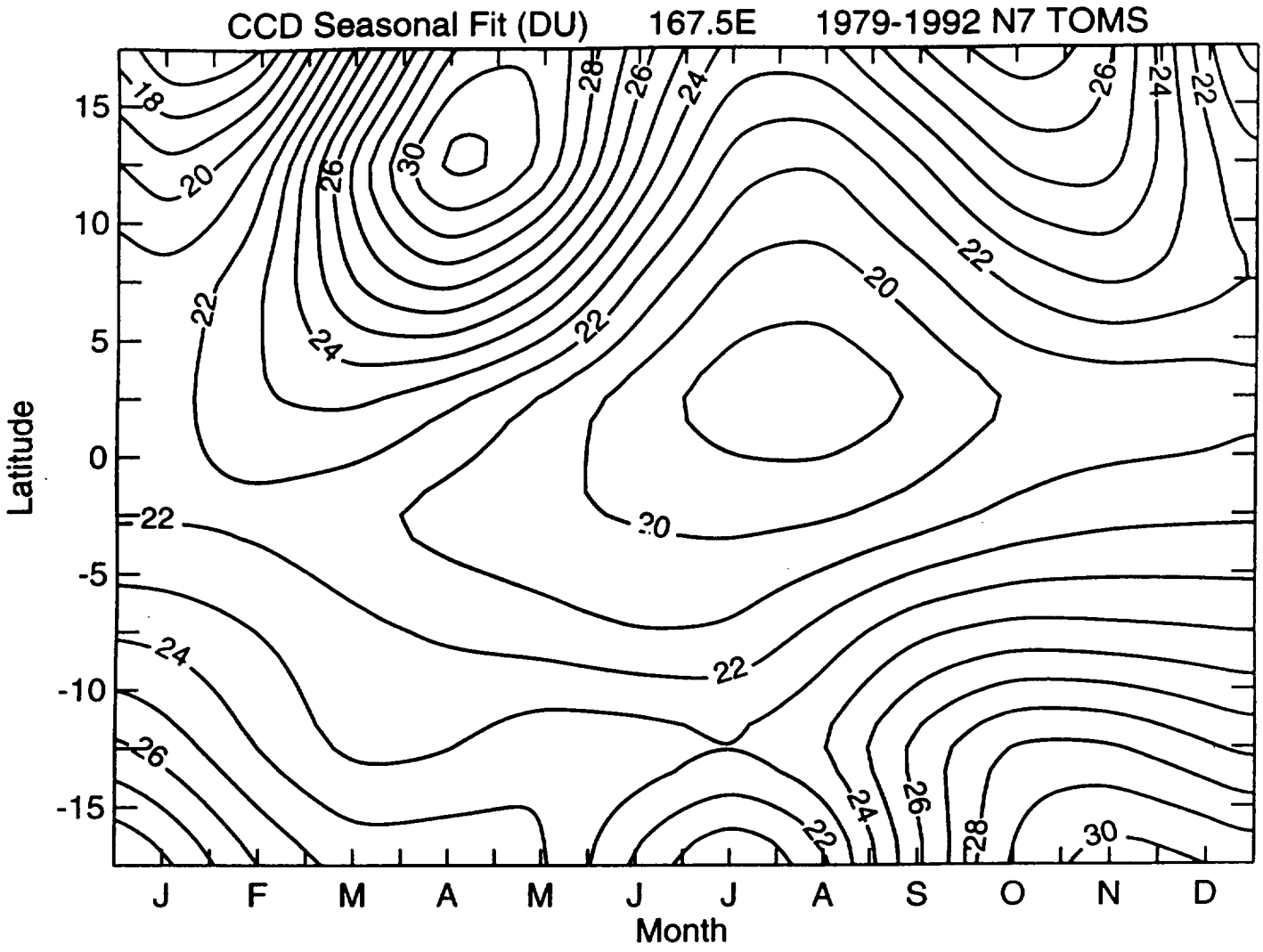
CCD Seasonal Fit (DU) 167.5E 1979-1992 N7 TOMS
Latitude
15
10
5
0
-5
-10
-15
J F M A M J J A S O N D
Month
18
20
22
24
26
28
30